Biosensors and Bioelectronics 130 (2019) 214–224

Contents lists available at ScienceDirect

Biosensors and Bioelectronics

journal homepage: www.elsevier.com/locate/bios

Facile and clean synthesis of dihydroxylatopillar[5]arene-stabilized gold nanoparticles integrated Pd/MnO_2 nanocomposites for robust and ultrasensitive detection of cardiac troponin I

Xingcan Qian[a,b], Xu Zhou[a,b], Xin Ran[a], Hangcheng Ni[c], Zhi Li[a], Qing Qu[b,*], Jun Li[a], Guanben Du[a], Long Yang[a,*]

[a] Key Laboratory for Forest Resources Conservation and Utilization in the Southwest Mountains of China, Ministry of Education, Yunnan Province Key Lab of Wood Adhesives and Glued Products, School of Materials Science and Engineering, Southwest Forestry University, Kunming 650224, China
[b] School of Chemical Science and Technology, Yunnan University, Kunming 650091, China
[c] Department of Chemistry and State Key Laboratory of Synthetic Chemistry, The Chinese University of Hong Kong, Hong Kong, China

ARTICLE INFO

Keywords:
Sandwich-type electrochemical immunosensor
Dihydroxylatopillar[5]arene
Molecular recognition
Cardiac troponin I

ABSTRACT

In this work, a novel, facile, clean synthesis of monodisperse Au nanoparticles (AuNPs) with an average diameter of 5 nm was achieved by reducing $HAuCl_4$ with dihydroxylatopillar[5]arene (2HP5) in basic solution without the use of harsh reagents and/or external energy. Accordingly, toluidine blue (TB), one electrochemcial indicator, could enter into the cavity of 2HP5 to fabricate host-guest complex through strong electrostatic interaction and charge-transfer interaction, which significantly enhanced the loading quantity of TB and effectively suppressed the leaking of TB resulting in an ultrasensitive and robust electrochemical response. More importantly, the integration of 2HP5-stabilized AuNPs and Pd-decorated MnO_2 nanocomposites (2HP5@Au-Pd/MnO_2) might usually obtain a novel functional-enhanced materials and lead to new properties and improving the analytical performance and robustness of electrochemical devices. Therefore, we construct a sandwich-type electrochemical immunosensor using TB-2HP5@Au-Pd/MnO_2 nanocomposites as the transducing materials for robust and ultrasensitive detection of cardiac troponin I (cTnI), a significant biomarker of acute myocardial infarction. As anticipated, this immunosensor had remarkable robustness, sensitivity, stability, specificity, and corresponded linearly to the concentration of cTnI over a wide range from 0.005 to 20 ng mL^{-1} with a low detection limit of 2 pg mL^{-1} (S/N = 3). The proposed electrochemical immunosensor showed acceptable recoveries in human serum, indicating that macrocycle-stabilized metal nanoparticle might be a promising emerging transducer material for the detection of biological markers.

1. Introduction

Gold nanoparticles (AuNPs) have received particular attention due to their unique optical/electrical properties and promising applications in catalysis (Chen and Goodman, 2008), sensing (Siwy et al., 2005), biomedicine (Dreaden et al., 2012), and nanoelectronic devices (Zheng et al., 2009). Numerous developed methods for the preparation of AuNPs, containing chemical reduction (Novo et al., 2008), external energy assisted synthesis (Teranishi et al., 2001; Shen et al., 2006), and seed-mediated growth (Murphy et al., 2005), are concentrated on regulating the nanoparticles' size, morphology, and surface functionality meeting the demands of different applications. However, in the process of preparation of AuNPs, the utilization of conventional harsh/explosive reducing agents such as $NaBH_4$, N_2H_4, and hydroxylamine might produce a potential biological and environmental hazard (Yang and Pan, 2012). What's more, to balance the van der Waals forces accountable for nanoparticle aggregation, various protecting agents, for example, surfactants (Murphy et al., 2005), organic molecules (Sun et al., 2013), polymers (Shan and Tenhu, 2007), protein (Cui et al., 2013), and dendrimers (Hu et al., 2014) have been usually employed. Unfortunately, the interaction between stabilizers and nanoparticles poses difficult problems in the following separation steps and thus apparently influences the material performances, as well as restricting their potential use. Based on the above considerations, developing a clean, simple, low-cost, and rapid preparation method for AuNPs with controlled particle size and morphology without the aid of reducing agents and/or external energy resources has stimulated significant interest.

* Corresponding authors.
E-mail addresses: quqing@ynu.edu.cn (Q. Qu), 133109070@126.com (L. Yang).

https://doi.org/10.1016/j.bios.2019.01.041
Received 6 November 2018; Received in revised form 16 January 2019; Accepted 18 January 2019
Available online 29 January 2019
0956-5663/

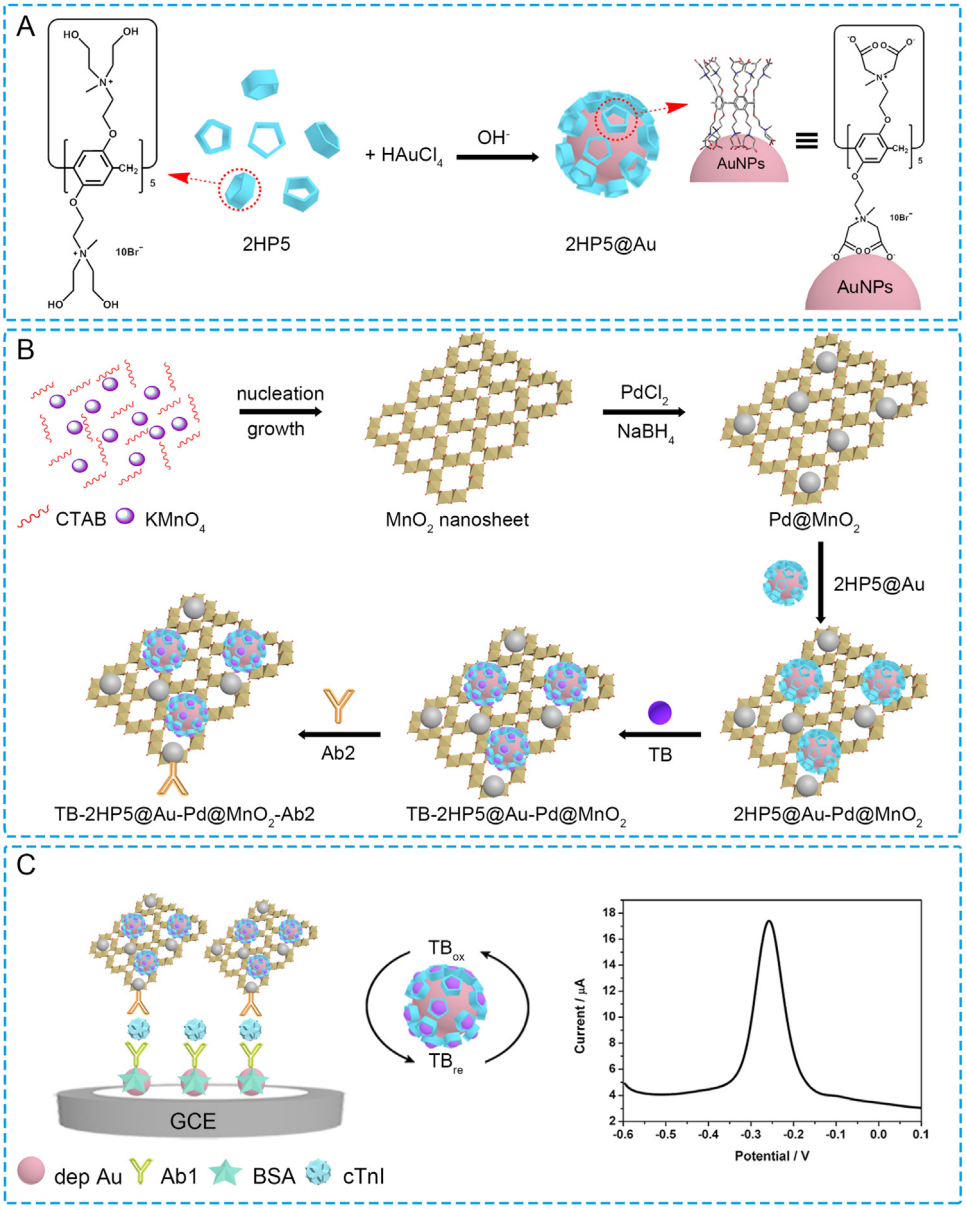

Scheme 1. The preparation process of 2HP5@Au (A), 2HP5@Au-Pd/MnO_2-Ab2 bioconjugates (B) and sandwich-type immunosensor (C).

Pillar[*n*]arenes, considered as the fifth-generation of macrocyclic hosts after crown ethers, cyclodextrins, calixarenes, and cucurbiturils, have repeating hydroquinone units linked by methylene bridges at their *para*-positions (Ogoshi et al., 2008). Owing to their intrinsic electron-rich cavity, symmetrical rigid pillar architecture, unique host-guest properties, and easy functionalization, pillar[*n*]arenes have been widely employed for the construction of various fascinating supramolecular strategies, including chem/bio sensors (Zhou et al., 2018), self-assembly (Yao et al., 2012), molecular recognition (Ogoshi et al., 2010), and separation (Fang et al., 2015). The introduction of specific functional groups into upper and/or lower rims of pillar[*n*]arenes, e.g., amine (Yao et al., 2013), sulfhydryl (Zhou et al., 2015), carboxyl (Li et al., 2013), have recently been proposed and developed as stabilizing ligands to synthesize AuNPs. But the reducing ability of pillar[*n*]arenes with reactive hydroxyl groups and their application in the synthesis of AuNPs have been relatively unexplored. Consequently, the preparation of AuNPs by the redox reaction between chloroauric acid and hydroxylatopillar[5]arene without any reducing reagents would be more environmentally friendly. Besides, the combination of metal nanoparticles and macrocyclic supramolecules simultaneously possess the host-guest recognition ability of pillar[*n*]arenes and the exclusive optical/electrical properties of AuNPs, and might result in significant synergistic effects and extending their applications.

Toluidine blue (TB), an accepted electrochemical redox probe, is extensively applied to immunosensor because of its notable electroconductivity, reversible electron-transfer ability, and high chemical stability (Xie et al., 2012; Peng et al., 2015). The leakage of electroactive mediator from electrode surface into solution remains a currently challenging problem, which can be effectively resolved through specific guest recognition of TB with pillar[*n*]arenes. The multiple interactions between macrocyclic supramolecules and dye molecules, for example, electrostatic interaction, π-π stacking, hydrogen bonding, and hydrophobic interaction (Dsouza et al., 2011), can motivate the guests enter into the cavity of hosts and therefore apparently promoted the loading amount of TB and effectively inhibited the leaking of TB resulting in an ultrasensitive and robust electrochemical response (Lin et al., 2013; Shen et al., 2015).

Acute myocardial infarction (AMI), medically called heart attack, has caused a severe global public health problem because the highest rates of morbidity and mortality (Kazemi et al., 2016). It occurs when

the blood circulation or flow suddenly stops to the coronary artery, resulting in ischemia, tissue damage, and even death (Chen et al., 2016). Real-time quantification of AMI biomarkers is significant for early diagnosis of disease, managing the treatment process, and assessment of therapeutic efficacy. Cardiac troponin I (cTnI), an essential myocardial regulatory protein in the cardiac muscle tissues, has been recognized as the sensitive and specific biomarkers in the diagnosis of AMI (Liu et al., 2016). Generally, the concentration of cTnI in healthy humans is below 0.4 ng mL^{-1} (Yan et al., 2018), while a rise in serum cTnI level is usually considered an increased risk of getting AMI. Various approaches have been explored for the measurement of cTnI, including enzyme-linked immunosorbent assay (Cho et al., 2009), electrochemiluminescence (Tang et al., 2018), electrochemical immunosensor (Yan et al., 2018) and fluorescence analysis (Seo et al., 2016). Among them, electrochemical immunosensor has stimulated a massive interest due to its rapid response, high sensitivity, and low cost. Despite numerous efforts have been made, improving the stability of sensing system to satisfy the needs of practical application is still being a considerable issue to explore and solve. Consequently, developing novel strategies and materials to construct an electrochemical immunosensor for cTnI detection have important value and significance.

In this work, we have synthesized a new water-soluble pillararenes (dihydroxylatopillar[5]arene, 2HP5) with abundant hydroxyl groups. Based on the strong reducing ability of -OH, a novel, facile, and clean method was established to prepare AuNPs without the use of harsh reagents and/or external energy. The formation mechanism of AuNPs was investigated using FTIR, XPS, and ^{13}C NMR techniques. Due to their excellent electrochemical properties, high specific surface area, and large number of active sites, MnO_2 nanosheets were introduced as a favorable supporting material for improving the loading amount of Pd (Z.M. Hu et al., 2015; Wei et al., 2014; Yang et al., 2018), which could immobilize detection antibody (Ab2) through Pd-N bond. Therefore, a sandwich-type electrochemical immunosensor was constructed by integrating 2HP5-stablized AuNPs and Pd-decorated MnO_2 nanocomposites (2HP5@Au-Pd/MnO_2), and the electrochemical response was produced through TB oxidation (Scheme 1). Because the strong electrostatic attraction and cooperative charge-transfer interaction between 2HP5 and TB, this immunosensor presented remarkable robustness, ultra-high sensitivity, notable stability and specificity, indicating the macrocycle-stabilized metal nanoparticle might be an emerging promising biomaterial for biomarkers detection.

2. Experimental

2.1. Materials

cTnI, primary antibodies (Ab1), and detection antibodies (Ab2), were purchased from Zhengzhou Biocell Biotechnology Co., Ltd. (China). Bovine serum albumin (BSA), potassium hexacyanoferrate (III) ($K_3Fe(CN)_6$), potassium hexacyanoferrate (II) ($K_4Fe(CN)_6{\cdot}3H_2O$), poly (ethylene glycol) (PEG 400), toluidine blue (TB), sodium citrate dihydrate ($Na_3C_6H_5O_7{\cdot}2H_2O$), sodium tetrahydroborate ($NaBH_4$), phosphate dodecahydrate (NaH_2PO_4), and sodium phosphate dibasic dodecahydrate ($Na_2HPO_4{\cdot}12H_2O$) were provided by Adamas-Beta Reagent (Shanghai, China). Hexadecyltrimethylammonium bromide (CTAB), gold chloride ($HAuCl_4{\cdot}4H_2O$), and palladium chloride ($PdCl_2$) were obtained from Sigma-Aldrich Chemical (America). 2HP5 was synthesized by introducing hydroxyl groups on the upper and lower rims, as demonstrated in Figs. S1–3. Ultrapure water with 18.25 MΩ cm was purified using a Millipore Milli-Q system.

2.2. Apparatus

The crystal structure of the synthesized materials were examined by X-ray diffractometry (XRD) collected on Rigaku TTR-III using Cu Kα radiation (Japan). Transmission electron microscope (TEM) was used to analyze the morphology, which was studied by a JEM-2100F microscope (Japan), as well as high-resolution TEM (HRTEM) and elemental mapping. The fluorescence and UV–vis absorption spectra were measured by F-4600 spectrometer (Japan) and Hitachi U-2900 spectrophotometer (Japan), respectively. Fourier transform infrared (FTIR) spectrum was recorded on a Thermo Nicolet iS10 spectrometer (America). X-ray photoelectron spectroscopy (XPS) of the samples were performed with a Thermo K-Alpha$^+$ spectrometer (America). ^1H NMR and ^{13}C NMR spectra were investigated with a Bruker AV. DRX5 instrument operated at 500 MHz. Electrochemical measurements were obtained from a CHI660E electrochemical workstation (Shanghai Chenhua Instrument Co. Ltd., China) with conventional three-electrode system, including a modified glassy carbon working electrode (GCE), a saturated calomel reference electrode (SCE) and a Pt wire auxiliary electrode.

2.3. Preparation of 2HP5@Au

In a typical synthesis, $HAuCl_4$ aqueous solution (255 μL, 10 mM) was mixed with an equimolar amount of 2HP5 aqueous solution in 2.0 mL of deionized water under continuously stirring at the ambient temperature. After NaOH aqueous solution (100 μL, 0.5 M) was added into the above mixture, the brownish-red solution immediately and completely turned colorless, and ultimately obtained a wine-red colored solution in a few minutes, illustrating the successful preparation of AuNPs. No lighting or heating required during the synthesis process. The solid powder was obtained by centrifuging, washing three times with water, and freeze-drying.

2.4. Preparation of Pd/MnO_2

MnO_2 nanosheets were prepared based on a typical hot-injection method (Wei et al., 2014). Generally, 0.9 g of CTAB was dissolved into 25 mL deionized water, followed by heating to 140 °C under the stirring condition. Then, $KMnO_4$ aqueous solution (25 mL, 20 mM) was rapidly added into the above solution maintaining the temperature constant until its color changed from purple to brown. MnO_2 nanosheets were separated with the addition of acetone, and purified by centrifugation, washing and freeze-drying.

The synthesis of the Pd/MnO_2 was as follows. Briefly, 20 mg of MnO_2 was dispersed into 10 mL deionized water, and subsequent addition of PEG 400 (100 μL), sodium citrate (1.0 mL, 10 mM), $PdCl_2$ aqueous solution (250 μL, 20 mM). After keeping constantly stirring for 2 h, $NaBH_4$ solution (3 mL, 15 mM) was added dropwise to the above mixture, continue stirring for 1 h. The obtained precipitate was centrifuged and washed with water three times, and then freeze-dried.

2.5. Preparation of TB-2HP5@Au-Pd/MnO_2

2HP5@Au-Pd/MnO_2 was synthesized by mixing 2HP5@Au solution with Pd/MnO_2 under continuous stirring overnight. The prepared nanocomposites were obtained by centrifuging, washing several times in water and drying.

The synthetic process of TB-2HP5@Au-Pd/MnO_2 was according to the following steps. The mixture of TB aqueous solution (2.0 mL, 2.5 mg mL^{-1}) and 2HP5@Au-Pd/MnO_2 solution (5.0 mL, 1.0 mg mL^{-1}) was vigorously stirred at room temperature for 12 h. The resultant products were collected from the suspension by repeatedly centrifuged and washed, and finally dispersed into pH 7.0 PBS (2.0 mL, 0.1 M). The actual samples of the synthesized nanomaterials were illustrated in Fig. S4.

2.6. Preparation of Ab2 bioconjugates

The cTnI detection antibodies (Ab2) conjugated TB-2HP5@Au-Pd/MnO_2 nanocomposites (Ab2 bioconjugates) were synthesized by adding

100 μL of 1.0 mg mL^{-1} Ab2 to the TB-2HP5@Au-Pd/MnO_2 solution and incubated at 4 °C overnight.

The above mixture was centrifuged and washed with PBS for 3 times, and lastly dispersed into PBS under refrigerated condition (4 °C).

2.7. Preparation of electrochemical immunosensor

The GCE was firstly polished by alumina powder and thoroughly washed with water. The AuNPs modified GCE (Au/GCE) was prepared by electrodepositing $HAuCl_4$ aqueous solution onto the surface of glassy carbon electrode (−0.2 V, 200 s). The Au/GCE was immersed into a primary antibodies (Ab1) solution (200 μL, 10 μg mL^{-1}) for 12 h at 4 °C to immobilize Ab1, the fabricated Ab1/Au/GCE was rinsed with PBS to remove the non-specific adsorption of Ab1. To close the remaining active sites, 10 μL of 2% BSA was dropped onto the previously modified electrode and rinsed. Then the BSA/Ab1/Au/GCE was incubated in different concentration of cTnI solution (0.005–20 ng mL^{-1}) at room temperature for 1 h to capture antigen. After washing, the sandwich immunosensor was completely constructed by adding 10 μL of Ab2 bioconjugates onto the cTnI/BSA/Ab1/Au/GCE, the obtained electrode (Ab2 bioconjugates/cTnI/BSA/Ab1/Au/GCE) was rinsed with PBS and stored at 4 °C. The preparation process of this sandwich-type electrochemical immunosensor was illustrated in Scheme 1.

2.8. Electrochemical measurements

The values of cyclic voltammetry (CV) and electrochemical impedance spectroscopy (EIS) were investigated in pH 7.0 PBS solution including 0.1 M KCl and 2 mM $[Fe(CN)_6]^{3-/4-}$. The CV responses were identified with a wide potential range from − 0.3–0.6 V and a scan rate of 50 mV s^{-1}. The EIS data was studied within the range of 0.1–10^5 HZ and the initial voltage was acquired by examining open circuit potential. Differential pulse voltammetry (DPV) was employed for cTnI detection by scanning the potential from − 0.6–0.1 V. Increment potential = 0.004 V, amplitude = 0.05 V, pulse width = 0.06 s, sample period = 0.02 s and pulse period = 0.5 s. These electrochemical experiments were performed at ambient temperature.

3. Results and discussion

3.1. Characterization of 2HP5@Au

AuNPs were facilely synthesized using 2HP5 molecules as reducing agents in alkaline condition without any external energy. The TEM and HRTEM images of 2HP5-stabilized AuNPs were shown in Fig. S5, as illustrated, these nanoparticles were principally spherical in shape and well-dispersed with distinct lattice fringes. Various characterization techniques have been applied to investigate the formation mechanism of AuNPs. The FTIR measurements of 2HP5 and 2HP5@AuNPs were firstly examined. As shown in Fig. 1A, the analogous portraits of two curves basically identified that the predominant feature groups of 2HP5 were maintained in the resultant products. What's more, a newly appeared absorption peak at 1729 cm^{-1} was attributed to C=O stretching vibration (J.Y. Hu et al., 2015), indicating the formation of carboxylate groups during the reaction process. The conclusion was further verified by comparing XPS data. From Fig. 1B, compared to that of pure 2HP5, the survey spectra of 2HP5@AuNPs confirmed the presence of Au elements, exhibiting that AuNPs were successfully prepared using 2HP5 as reducing agents. The comparison of C 1 s and O 1 s spectrum between pure 2HP5 (Fig. 1C and D) and 2HP5@AuNPs (Fig. 1E and F) similarly suggested the existence of C=O groups in products. Significantly, the hydroxyl groups in 2HP5@AuNPs were apparently lower than that of pure 2HP5, along with the appearance of carboxyl groups, demonstrating that hydroxyl groups in 2HP5 could reduce the Au precursor to Au, and their own were oxidized to carboxylic acid. Moreover, the results of ^{13}C NMR (125 MHz, D_2O) in Fig. 1G were consistent with FTIR and XPS. As described, a new carboxyl group presented at 168.26 ppm in ^{13}C NMR spectra of 2HP5@AuNPs were corresponded to C=O bonds.

Based on these findings, we speculated a possible reduction mechanism of AuNPs using 2HP5 as reducing agents in alkaline condition. $[AuBr_4]^-$ was firstly produced when 2HP5 solution was added into $HAuCl_4$ aqueous solution, because the dissociation constants of $[AuBr_4]^-$ was far less than that of $[AuCl_4]^-$ (Usher et al., 2009). However, the addition of NaOH caused the mixture solution moderately basic, the $[AuBr_4]^-$ complex immediately disassembled and resulted in the formation of $[Au(OH)_4]^-$ (Oyaizu et al., 2005). Another important role of NaOH was connected with the movement of the reaction equilibrium. As previously mentioned, when Au precursor was reduced and formed Au by the hydroxyl groups of 2HP5, the protons were also produced and quickly neutralized and vanished by hydroxyl ions from NaOH, resulting in the reduction rate to be facilitated based on Le Chatelier's principle (Tang et al., 2013). Moreover, the oxidation products of 2HP5 containing many carboxyl groups with negative charge would cover the AuNPs surface by Au-COO^- interaction, and inhibit unrestricted growth and/or agglomeration of nanoparticles.

3.2. Characterization of 2HP5@Au-Pd/MnO_2

Fig. 2A and B respectively showed the typical TEM and HRTEM images of the prepared MnO_2 nanosheets, which suggested that nanosheets were uniform lamellar structure with apparent lattice fringes. The Pd/MnO_2 nanocomposites were synthesized by reducing PdNPs on MnO_2 nanosheets, and their morphology was illustrated in Fig. 2C and D. As presented, the abundant spherical Pd nanoparticles were uniformly monodispersed on the surface of MnO_2. The TEM images of prepared 2HP5@Au-Pd/MnO_2 nanocomposites described 2HP5-stabilized AuNPs were successfully anchored onto the Pd/MnO_2 surface (Fig. 2E and F). From the inset HRTEM image in Fig. 2G, the interplanar spacing of 0.230 nm belonging to Pd{111} faces (Fu et al., 2013), and 0.235 nm attributing to Au{111} faces (Li et al., 2013).

2HP5@Au-Pd/MnO_2 was further identified by elemental mapping experiments to determine the combination of 2HP5@Au and Pd/MnO_2. As described in Fig. S6, the results confirmed the distribution of Mn, Au, Pd, O, and N elements on the composites, where N was come from 2HP5. The crystalline structure of 2HP5@Au-Pd/MnO_2 was also investigated and shown in Fig. S7, for comparison, the XRD pattern of MnO_2 and Pd/MnO_2 were also studied. For MnO_2 nanosheets, the characteristic diffraction peaks of {110}, {200}, {211}, and {002} crystal facets were emerged clearly, which were belonged to tetragonal crystalline phase (JCPDS 44–0141). Compared to pure MnO_2 nanosheets, the diffraction intensity of Pd in Pd/MnO_2 was much weaker, owing to the relatively small amount and size of PdNPs (Wilson et al., 2002). With the introduction of 2HP5@Au, two distinct diffraction peak at 38.3° and 65.3° were emerged corresponding to Au{111} and Au{220} faces (Imura et al., 2011), demonstrating that 2HP5@Au was successfully attached onto Pd/MnO_2 nanosheets.

Because the elements of Au and Pd in 2HP5@Au-Pd/MnO_2 composites could not be obviously observed by elemental mapping and XRD results, thus, XPS measurement was employed to characterize the surface chemical composition of the composites. As shown in Fig. 3A, the XPS survey spectrum suggested the existence of Mn, O, N, Pd, C, and Au elements in 2HP5@Au-Pd/MnO_2. The C 1s XPS spectrum (Fig. 3B) exhibited five kinds of carbon atoms, C-C (284.7 eV), C-N (285.1 eV), C-O (286.1 eV), C=O (287.4 eV), and O-C=O (288.4 eV), while the O 1 s spectrum (Fig. 3C) displayed four types, O-Mn (530.2 eV), *O=C-O (531.4 eV), O-C (532.4 eV), and *O-C=O (533.5 eV), respectively (Chen et al., 2014; de Godoi et al., 2013; Yan et al., 2016; Zhao et al., 2018). Fig. 3D demonstrated that the intensive peaks for Au 4f were centered at 87.4 eV ($4f_{5/2}$) and 83.7 eV ($4f_{7/2}$), and the binding energies of Pd $3d_{3/2}$ and Pd $3d_{5/2}$ in Fig. 3E were located at 340.5 eV and 335.3 eV (Yang et al., 2013). As displayed in Fig. 3F, the Mn $2p_{1/2}$ peak at 654.0 eV and Mn $2p_{3/2}$ peak at 642.3 eV with the spin-energy

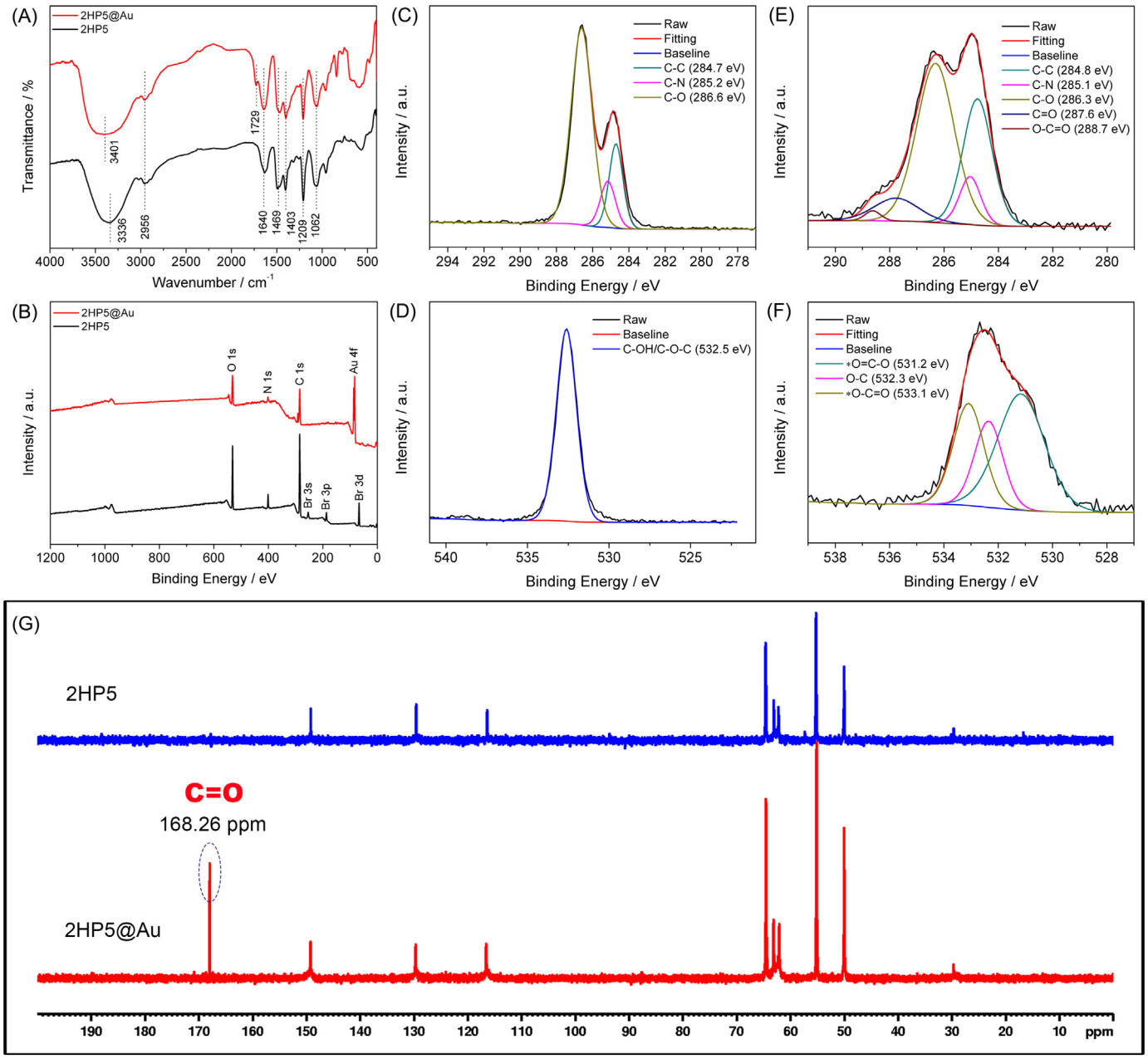

Fig. 1. FTIR (A) and XPS (B) spectra of 2HP5 and 2HP5@Au; high-resolution XPS of C 1s (C) and O (D) 1s in 2HP5; high-resolution XPS of C 1s (E) and O (F) 1s in 2HP5@Au; ^{13}C NMR spectra (125 MHz, D_2O) of 2HP5 and 2HP5@Au (G).

separation of 11.7 eV were confirmed the 4 + oxidation state of Mn (Sun et al., 2017).

3.3. Host-guest recognition studies

The complexation between 2HP5@Au and TB was firstly investigated by UV–vis experiments. As illustrated in Fig. 4A, TB produced a significant absorption peak at 632 nm (Saito et al., 2011). Upon the addition of 2HP5@Au, the UV–vis adsorption intensities of TB were gradually decreased and an apparent red shift could be observed, demonstrating the formation of host-guest complex 2HP5@Au⊃TB, which were primarily driven by electrostatic attraction and cooperative charge-transfer interaction between host and guest (Hua et al., 2018). What's more, a control experiment was conducted to demonstrate that the decrease of TB's adsorption peak was caused by the host-guest recognition between TB and the oxidation products of 2HP5, rather than the interaction of Au with TB. For comparison, Au nanoparticles were synthesized through citrate-stabilized methods (Bastús et al., 2011). From Fig. S8, there was no obvious change of the adsorption peak intensity upon the continuous addition of citrate-stabilized AuNPs in TB solution. Based on the above experimental results, we confirmed the inclusion of TB into the cavity of 2HP5@Au.

The association constant (K_a) of 2HP5@Au⊃TB complex was obtained from fluorescence spectroscopy data. Fig. 4B showed the fluorescence intensities of TB in the absence and presence of 2HP5@Au, which was consistent with the UV–vis spectra. A mole ratio plot based on fluorescence titration measurements investigated the complex between 2HP5@Au and TB had 1:1 stoichiometry (Fig. 4C), and K_a was determined to be (6.95 ± 0.24) × 10^4 M^{-1} using Stern-Volmer formulation (Fig. 4D).

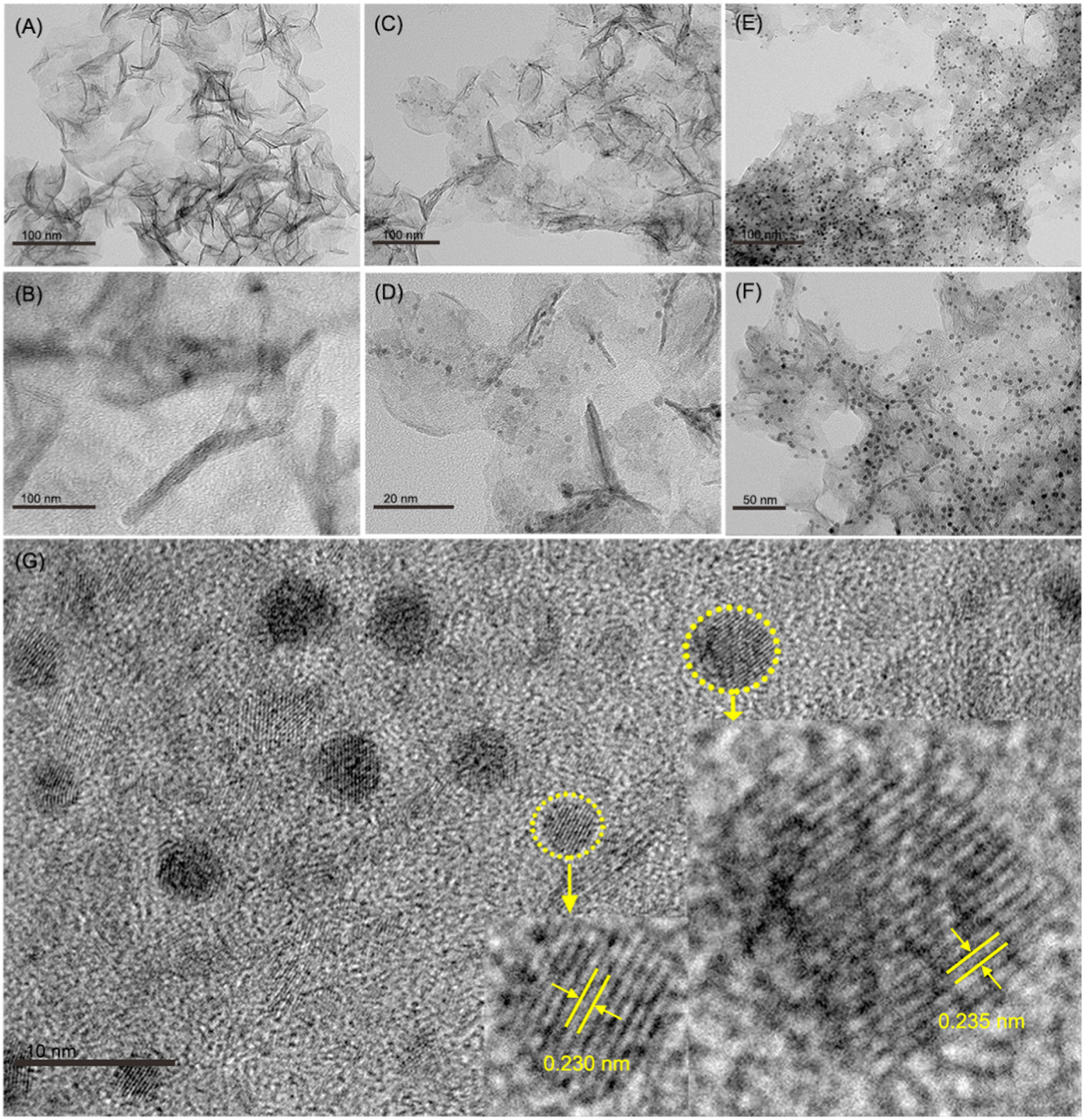

Fig. 2. TEM (A) and HRTEM (B) images of MnO_2; TEM (C) and HRTEM (D) images of Pd/MnO_2; TEM (E) and HRTEM (F) images of 2HP5@Au-Pd/MnO_2; the inset of part F displayed the lattice spacing of the AuNPs and PdNPs were 0.235 nm and 0.230 nm, respectively (G).

3.4. Characterization of immunosensor

The stepwise fabrication process of immunosensor was characterized by CV measurements and the results were illustrated in Fig. 5A. The CV curve of bare GCE displayed a couple of well-defined redox peaks belonging to $[Fe(CN)_6]^{3-/4-}$. Compared with GCE, the electrochemical response significantly increased when gold nanoparticles were electrodeposited on the electrode because the AuNPs could accelerate the electron transfer. The Au/GCE was applied to immobilize Ab1 through the interaction of Au-NH_2 (Zhao et al., 2016), and the peak current of Ab1/Au/GCE was greatly decreased due to the non-conductive properties of proteins, which inhibited the electron transfer. Equally, the current response was further decreased when the Ab1/Au/GCE was sequentially combined with BSA and cTnI. Finally, when TB-2HP5@Au-Pd/MnO_2 labeled Ab2 was modified on the prepared electrode (cTnI/BSA/Ab1/Au/GCE), a notably enhanced current was achieved, indicating that cooperative effects between large specific surface area of MnO_2 nanosheets, and excellent electrical conductivity of AuNPs and PdNPs. The corresponding current changes in the voltammogram determined the successful preparation of the sandwich-type immunosensor.

EIS measurements were further employed to confirm the interface

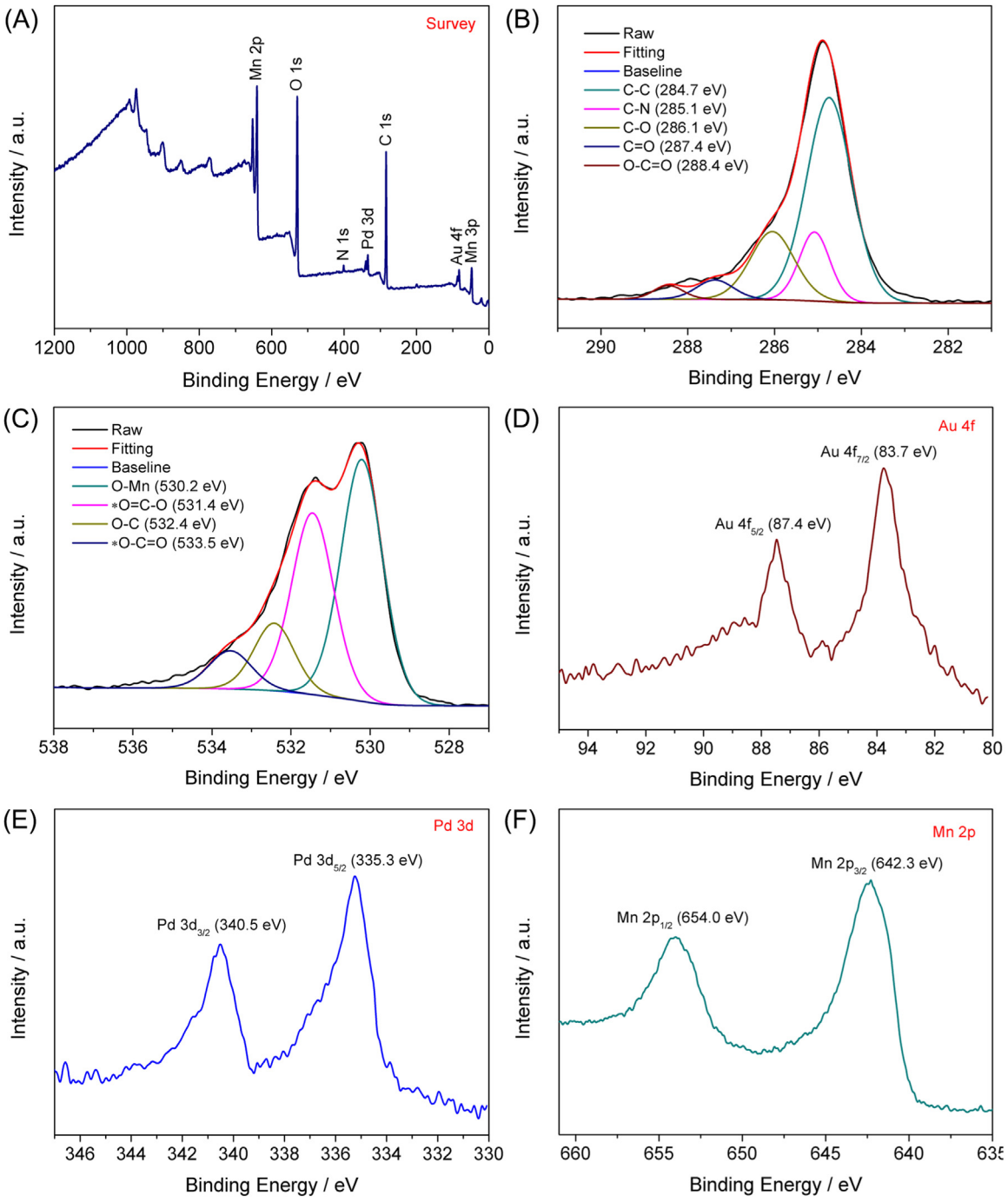

Fig. 3. XPS spectra of 2HP5@Au-Pd/MnO_2; high-resolution XPS of C 1s (B), O 1s (C), Au 4f (D), Pd 3d (E), and Mn 2p (F).

properties of the fabricated electrodes at each modification steps. The impedance spectra contained a semicircle part at higher frequencies corresponding to the electron-transfer resistance (R_{et}) and a linear part at lower frequencies belonging to diffusion-limited process (Zhang et al., 2014). From Fig. 5B, after modified with Au nanoparticles, the semicircle diameter on impedance spectra could hardly be observed, suggesting an ignorable impedance because AuNPs with outstanding electroconductivity could enhance the electron transfer and thus hold smaller resistance. But the resistance values were gradually increased when the Au/GCE was coated with Ab1 (Ab1/Au/GCE), BSA (BSA/Ab1/Au/GCE), and cTnI (cTnI/BSA/Ab1/Au/GCE), which could be attributed to the biological substances significantly inhibited the electron transfer rate. As expected, with the Ab2 bioconjugates coated on the further resultant electrode, the R_{et} value apparently decreased because of strong adsorption ability of MnO_2 nanosheets towards $[Fe(CN)_6]^{3-/4-}$ and favorable conductivity of noble metal nanoparticles in the TB-2HP5@Au-Pd/MnO_2. Therefore, both CV and EIS results displayed the successful assembly of this immunosensor.

3.5. Optimization of experimental conditions

The external experimental conditions, which might influence the sensitivity and sensing performance of electrochemical immunosensor, are necessary to be optimized. On the basis of the above-mentioned consideration, these optimization measurements were carried out using DPV technique, and the concentration of cTnI was 1.0 ng mL^{-1}. The pH

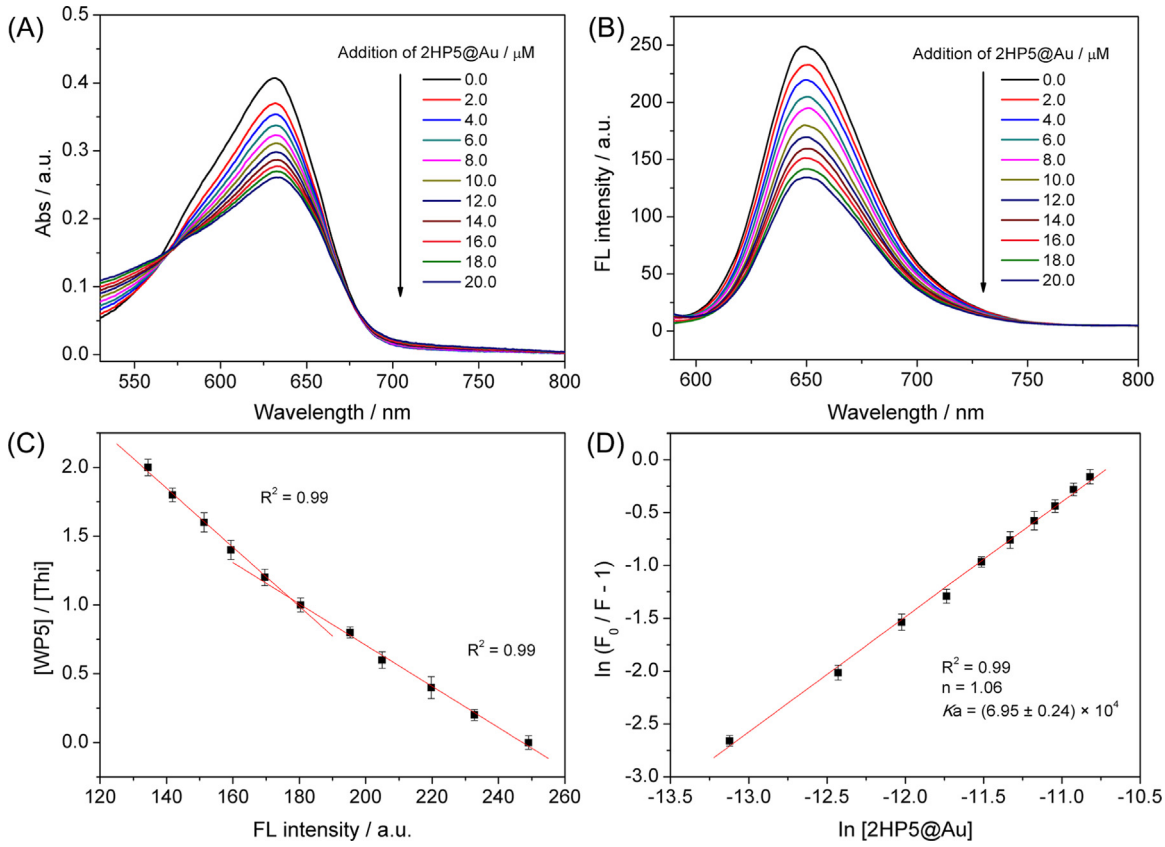

Fig. 4. UV–vis (A) and fluorescence (B) spectra of 10 μM TB in the presence of 0, 0.2, 0.4, 0.6, 0.8, 1.0, 1.2, 1.4, 1.6, 1.8 and 2.0 equivalent of 2HP5@Au in aqueous solution; mole ratio plot demonstrating 1:1 stoichiometry of 2HP5@Au ⊃ TB complex (C); the Stern-Volmer plots of $\ln(F_0/F - 1)$ versus In [2HP5@Au], where F_0 is the initial fluorescent intensity of TB and F is the fluorescent intensity of TB under the existence of different concentrations of 2HP5@Au.

value of detection solution was firstly examined because alkaline or acid solutions might dissociate the antigen-antibody complex, as well as influence the biological activity of proteins (Shen et al., 2015). Fig. 5C showed the DPV responses of TB-2HP5@Au-Pd/MnO_2 in PBS at different pH solution. The peak current persistently increased with changing pH from 5.5 to 7.0, and decreased when pH was higher than 7.0. Therefore, detection solution of pH 7.0 was chosen for the following experiments.

The concentration of TB-2HP5@Au-Pd/MnO_2 was another influential factor that affect the electrochemical response. As described in Fig. 5D, the peak currents were recorded at different concentration of Ab2 bioconjugates in 7.0 PBS. The DPV currents correspondingly improved with the variation of concentration from 0.6 to 1.6 mg mL^{-1}, and then remained stable when we continued to increase concentrations. The response variations suggested that the optimized concentration of TB-2HP5@Au-Pd/MnO_2 was 1.6 mg mL^{-1}.

The effect of recovery time on the analyte-electrode should also be considered. According to the literature, the recovery time is calculated by the following equation: recovery time = pulse period - pulse width (Tachikawa et al., 1986). The variation of the electrochemical response with recovery time is presented in Fig. S9. As illustrated, the optimized recovery time of immunosensor is 0.44 s. Thus, the recovery time of 0.44 s was applied in the following experiments.

3.6. Performance of immunosensor

Under optimized experiment conditions, the sandwich-type electrochemical immunosensor using TB-2HP5@Au-Pd/MnO_2 as labels was applied to quantitatively determine cTnI by DPV investigation. Fig. 5E presented the DPV current responses of the fabricated immunosensor for detection of antigen covering the concentration range from 0.005 to 20 ng mL^{-1}. With the increase of the cTnI concentration, more antigens were specifically recognized by antibodies, and result in the sequentially increasing of electrochemical current. The blank sample was obtained by incubating with 0 ng mL^{-1} of cTnI, which had a neglectable current signal, indicating that the influence of non-specific adsorption on this immunosensor could be ignored. As Fig. 5F illustrated, a linear relationship between response variations and the logarithm of cTnI concentration was acquired in the range of 0.005–20 ng mL^{-1}, with lower detection limit of 0.002 ng mL^{-1} (signal/noise = 3). The linear regression equation was I = 5.989 logC + 18.08 with correlation coefficient of 0.9951, where I was current response and C was cTnI concentration.

Compared with previous methods (summarized in Table S1), this immunosensor presented a wider linear range and lower detection limit. The outstanding sensing performance of the as-proposed method was attributed to the signal amplification of TB-2HP5@Au-Pd/MnO_2. As mentioned above, the peak current was predominantly produced by the oxidation reaction of TB. The host-guest recognition interaction between 2HP5@Au and TB not only enhanced the loading amount of electroactive molecules but also improved the stability of immobilized TB through electrostatic attraction and cooperative charge-transfer interaction, which could stable and increase the electrochemical signal. What's more, the introduction of noble metal nanoparticles with remarkable electroconductivity and favorable biocompatibility such as Au and Pd could accelerate electron transfer and broaden the detection range (Li et al., 2017). Besides, MnO_2 nanosheets as supporting material provided larger specific surface areas and more active sites for nanoparticles, which further increased the electrochemical response.

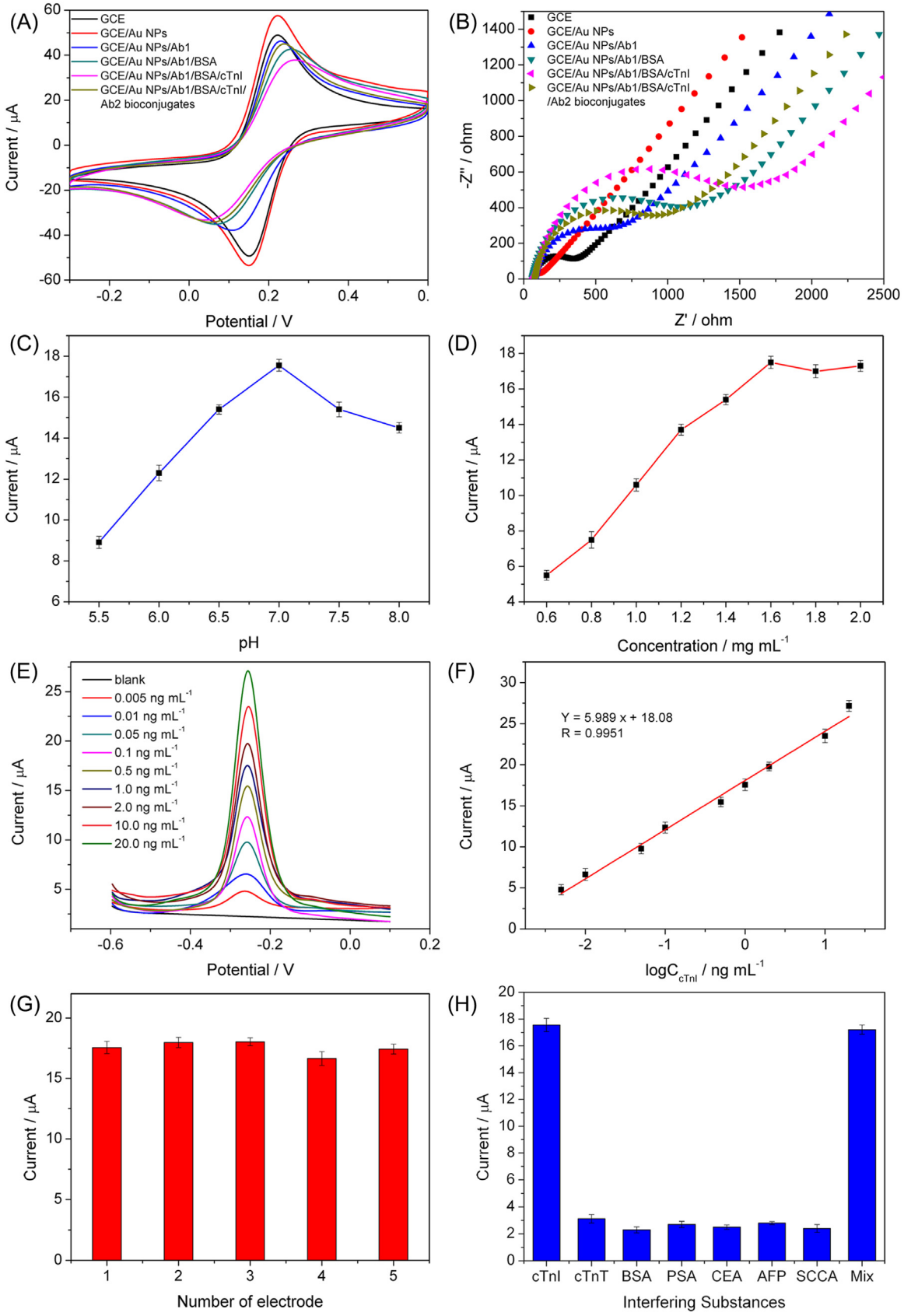

Fig. 5. CV (A) and EIS (B) of stepwise fabricated electrodes in 7.0 PBS including 0.1 M KCl and 2 mM K_3/K_4 $Fe(CN)_6$; the optimized experimental conditions of pH (C) and Ab2 conjugates concentration (D); DPV current (E) of this immunosensor towards different cTnI concentrations (0.005 ng mL^{-1} to 20 ng mL^{-1}); linear relationship between DPV response variation and the logarithm of cTnI concentration (F); reproducibility (G) and specificity (H) of the proposed immunosensor.

3.7. Reproducibility, specificity, and stability of immunosensor

The reproducibility of electrochemical immunosensor has great significance for practical applications. To investigate the reproducibility of this immunosensor, five different working electrodes were applied for analyzing the same concentration of cTnI (1.0 ng mL^{-1}) under optimal conditions. These five electrodes displayed approximately similar peak currents (Fig. 5G), and the relative standard deviation (RSD) of five experiments was 3.17%, which suggested that this immunosensor had an acceptable reproducibility for cTnI detection.

In order to determine the specificity of immunosensor, some possible interfering substances in human serum such as cardiac troponin T (cTnT), bovine serum albumin (BSA), prostate specific antigen (PSA), carcinoembryonic antigen (CEA), α − 1-fetoprotein (AFP), and squamous cell carcinoma antigen (SCCA) were employed. The concentration of cTnI was 1.0 ng mL^{-1}, while the interferences concentration was 10 ng mL^{-1}. As shown in Fig. 5H, the current response of cTnI immunosensor is much better than that of other proteins. This is mainly because other proteins cannot bind to cTnI antibodies (Ab1 or Ab2), and these unbound Ab2 conjugates were washed out. What's more, the response current of the co-existence of cTnI with these interferents has no obvious signal variation, indicating other proteins have little effect to the selectivity of cTnI immunosensor. To further verify the accuracy of the results, a complex system of serum was applied for the selective experiment of the immunosensor. The results have been presented in Fig S10. As shown, the other proteins based immunosensor did not cause an obvious electrochemical current compared with that of cTnI. The results further illustrates that the proposed immunosensor has a favorable selectivity and specificity. Compared with label-free immunosensor, the sandwich-type immunosensor has better selectivity and anti-interference ability due to the excellent specific recognition ability between Ab1-cTnI-Ab2. In order to demonstrate anti-interference ability of the immunosensor to interferents in serum, the additional experiments have been carried out. The serum sample was diluted with PBS buffer in different proportions (1:1, 1:2, 1:5, 1:10). The concentration of cTnI is 1.0 ng mL^{-1}, and the current response was measured by DPV method. The results are illustrated in Fig S11. As shown, there is no significant difference in the current values of serum solutions with different dilution rates, indicating that the amount of non-specific proteins adsorbed on the electrode interface is very small and the effect of non-specific adsorption of complex components in serum on the performance of the immunosensor is little. It was further found that when the concentration of cTnI was as low as 0.05 ng mL^{-1}, the electrochemical signal of the immunosensor in PBS is similar to that in serum (Fig S12). The above results show that the immunosensor have good selectivity and anti-interference ability.

The as-prepared immunosensor was further examined for its stability by measuring DPV current every five days. The modified working electrodes were stored at 4 °C before use and the results were obtained in Fig. S13. There was no distinct peak current variation of immunosensor after the first five days. Then the DPV signal declined sequentially and remained 88.1% of its initial value after a month, which suggested that the stability of this immunosensor was desirable. Compared to some reported immunosensor, the proposed method illustrated satisfying stability, which were attributed to the unique biocompatibility, remarkable host-guest recognition ability, and splendid chemical stability of TB-2HP5@Au-Pd/MnO_2 nanocomposites, resulting in sensitive and robust current response and further improving the sensing performance of immunosensor.

3.8. Analysis of cTnI in human serum

To examine the precision and reliability of the proposed sandwich-type immunoassay, the recoveries of different concentrations of cTnI (0.1, 0.5, 1.0, 2.0, and 5.0 ng mL^{-1}) in the serum samples were determined using standard addition method. As presented in Table S2, the recoveries of the two concentrations range from 95.8% to 103.0%, and the RSD was lower than 5.1% (n = 5). The measurement results demonstrated the fabricated immunosensor could accurately and efficiently analyze the cTnI concentration in real sample, which might have an appreciable application potential for clinical practice.

To further investigate the applicability of the fabricated sandwich-type electrochemical immunosensor, a comparison with enzyme-linked immunosorbent assay (ELISA) method was presented in Table S3. The results summarized a good correlation between the two analytical methods, and the relative errors for cTnI detection was below 3.5%, suggesting that the proposed method was reliable and efficient enough for clinical analysis.

4. Conclusions

In conclusion, a facile, green and clean preparation method of monodisperse AuNPs with the average size of 5 nm was developed by the redox reaction between $HAuCl_4$ and 2HP5 aqueous solution in alkaline conditions without the use of harsh reagents and/or external energy. The FTIR, XPS, and ^{13}C NMR experiments suggested the formation mechanism of AuNPs, and the formed carboxyl groups in 2HP5 oxidation products would cover the AuNPs surface by Au-COO^- interaction, which inhibit the unlimited growth and/or agglomeration of nanoparticles. Based on the electroconductivity properties and excellent host-guest recognition abilities of 2HP5@Au towards TB, a sandwich-type electrochemical immunosensor was constructed using Pd/MnO_2 nanosheets integrated 2HP5 @Au (2HP5@Au- Pd/MnO_2) as signal amplification labels. Due to the strong electrostatic attraction and cooperative charge-transfer interaction between macrocyclic hosts and toluidine blue molecules, the fabricated immunosensor produced sensitive and robust TB oxidation response, and thus presented remarkable sensing performance for detection of cTnI, as well as outstanding reproducibility, selectivity, stability, and potential feasibility. In the future work, we will focus on the integration of low-fouling nanomaterials and molecular recognition in electrochemical platforms for further improving their antifouling effects, robustness, and sensing performance.

CRediT authorship contribution statement

Xingcan Qian: Investigation, Writing - original draft, Writing - review & editing. **Xu Zhou:** Validation, Writing - review & editing. **Xin Ran:** Resources, Supervision. **Hangcheng Ni:** Resources, Supervision. **Zhi Li:** Resources. **Qing Qu:** Funding acquisition, Methodology. **Jun Li:** Supervision. **Guanben Du:** Funding acquisition, Supervision. **Long Yang:** Conceptualization, Funding acquisition.

Acknowledgements

This work was financially supported by the National Natural Science Foundation of China under the Grant No. 21864024, 51661033, 31660538, and the Program for Leading Talents, Yunnan Provincial Science and Technology Department, China (grant no. 2017HA013).

Conflict of interest

The authors declare no competing interests.

Appendix A. Supplementary material

Supplementary data associated with this article can be found in the online version at https://doi.org/10.1016/j.bios.2019.01.041.

References

Bastús, N.G., Comenge, J., Puntes, V., 2011. Langmuir 27, 11098–11105.
Chen, M.S., Goodman, D.W., 2008. Chem. Soc. Rev. 37, 1860–1870.
Chen, X.X., Jin, Q.Q., Wu, L.Z., Tung, C.H., Tang, X.J., 2014. Angew. Chem. Int. Ed. 53, 12542–12547.
Chen, G.F., Shen, Y.L., Xu, T.Z., Ban, F.F., Yin, L., Xiao, J.J., Shu, Y.Q., 2016. Biosens. Bioelectron. 77, 1020–1025.
Cho, I.H., Paek, E.H., Kim, Y.K., Kim, J.H., Paek, S.H., 2009. Anal. Chim. Acta 632, 247–255.
Cui, M.L., Liu, J.M., Wang, X.X., Lin, L.P., Jiao, L., Zheng, Z.Y., Zhang, L.H., Jiang, S.L., 2013. Sens. Actuators B 188, 53–58.
de Godoi, F.C., Rodriguez-Castellon, E., Guibal, E., Beppu, M.M., 2013. Chem. Eng. J. 234, 423–429.
Dreaden, E.C., Alkilany, A.M., Huang, X.H., Murphy, C.J., ElSayed, M.A., 2012. Chem. Soc. Rev. 41, 2740–2779.
Dsouza, R.N., Pischel, U., Nau, W.M., 2011. Chem. Rev. 111, 7941–7980.
Fang, Y.Y., Yuan, X.Y., Wu, L., Peng, Z.Y., Feng, W., Liu, N., Xu, D.G., Li, S.J., Sengupta, A., Mohapatra, P.K., Yuan, L.H., 2015. Chem. Commun. 51, 4263–4266.
Fu, G.T., Tao, L., Zhang, M., Chen, Y., Tang, Y.W., Lin, J., Lu, T.H., 2013. Nanoscale 5, 8007–8014.
Hu, D.M., Huang, Y.P., Liu, H., Wang, H., Wang, S.G., Shen, M.W., Zhu, M.F., Shi, X.Y., 2014. J. Mater. Chem. A 2, 2323–2332.
Hu, Z.M., Xiao, X., Huang, L., Chen, C., Li, T.Q., Su, T.C., Cheng, X.F., Miao, L., Zhang, Y.R., Zhou, J., 2015a. Nanoscale 7, 16094–16099.
Hu, J.Y., Lei, G., Lu, Z.G., Liu, K.Y., Sang, S.B., Liu, H.T., 2015b. Chem. Commun. 51, 9983–9986.
Hua, B., Shao, L., Zhang, Z.H., Sun, J.F., Yang, J., 2018. Sens. Actuators B 255, 1430–1435.
Imura, Y., Tanuma, H., Sugimoto, H., Ito, R., Hojo, S., Endo, H., Morita, C., Kawai, T., 2011. Chem. Commun. 47, 6380–6382.
Kazemi, S.H., Ghodsi, E., Abdollahi, S., Nadri, S., 2016. Mater. Sci. Eng. C 69, 447–452.
Li, H., Chen, D.X., Sun, Y.L., Zheng, Y.B., Tan, L.L., Weiss, P.S., Yang, Y.W., 2013. J. Am. Chem. Soc. 135, 1570–1576.
Li, Y.Y., Zhang, Y.H., Li, F.Y., Feng, J.H., Li, M.D., Chen, L., Dong, Y.H., 2017. Biosens. Bioelectron. 92, 33–39.
Lin, D.J., Wu, J., Ju, H.X., Yan, F., 2013. Biosens. Bioelectron. 45, 195–200.
Liu, G.Z., Qi, M., Zhang, Y., Cao, C.M., Goldys, E.M., 2016. Anal. Chim. Acta 909, 1–8.
Murphy, C.J., Sau, T.K., Gole, A.M., Orendorff, C.J., Gao, J.X., Gou, L.F., Hunyadi, S.E., Li, T., 2005. J. Phys. Chem. B 109, 13857–13870.
Novo, C., Funston, A.M., Mulvaney, P., 2008. Nat. Nanotechnol. 3, 598–602.
Ogoshi, T., Kanai, S., Fujinami, S., Yamagishi, T.A., Nakamoto, Y., 2008. J. Am. Chem. Soc. 130, 5022–5023.
Ogoshi, T., Hashizume, M., Yamagishi, T.A., Nakamoto, Y., 2010. Chem. Commun. 46, 3708–3710.
Oyaizu, K., Ohtani, Y., Shiozawa, A., Sugawara, K., Saito, T., Yuasa, M., 2005. Inorg. Chem. 44, 6915–6917.
Peng, H.P., Hu, Y., Liu, P., Deng, Y.N., Wang, P., Chen, W., Liu, A.L., Chen, Y.Z., Lin, X.H., 2015. Sens. Actuators B 207, 269–276.
Saito, T., Uematsu, T., Kimura, S., Enomaea, T., Isogai, A., 2011. Soft Matter 7, 8804–8809.
Seo, S.M., Kim, S.W., Park, J.N., Cho, J.H., Kim, H.S., Paek, S.H., 2016. Biosens. Bioelectron. 83, 19–26.
Shan, J., Tenhu, H., 2007. Chem. Commun. 44, 4580–4598.
Shen, M., Du, Y.K., Hua, N.P., Yang, P., 2006. Powder Technol. 162, 64–72.
Shen, W.J., Zhuo, Y., Chai, Y.Q., Yang, Z.H., Han, J., Yuan, R., 2015. ACS Appl. Mater. Interfaces 7, 4127–4134.
Siwy, Z., Trofin, L., Kohli, P., Baker, L.A., Trautmann, C., Martin, C.R., 2005. J. Am. Chem. Soc. 127, 5000–5001.
Sun, J., Yue, Y., Wang, P., He, H.L., Jin, Y.D., 2013. J. Mater. Chem. C 1, 908–913.
Sun, S.Q., Jiang, G.H., Liu, Y.K., Zhang, Y., Zhou, J.Y., Xu, B., 2017. Mater. Lett. 197, 35–37.
Tachikawa, M., Tanii, K., Kajita, M., Shimizu, T., 1986. Appl. Phys. B 39, 83–90.
Tang, J.Q., Huang, J.M., Man, S.Q., 2013. Spectrochim. Acta A 103, 349–355.
Tang, M., Zhou, Z.X., Shangguan, L., Zhao, F., Liu, S.Q., 2018. Talanta 180, 47–53.
Teranishi, T., Hasegawa, S., Shimizu, T., Miyake, M., 2001. Adv. Mater. 13, 1699–1701.
Usher, A., McPhail, D.C., Brugger, J., 2009. Geochim. Cosmochim. Acta 73, 3359–3380.
Wei, C., Yu, L.H., Cui, C.L., Lin, J.D., Wei, C., Mathews, N., Huo, F.W., Sritharan, T., Xu, Z.C., 2014. Chem. Commun. 50, 7885–7888.
Wilson, G.J., Will, G.D., Frost, R.L., Montgomery, S.A., 2002. J. Mater. Chem. 12, 1787–1791.
Xie, S.B., Yuan, R., Chai, Y.Q., Bai, L.J., Yuan, Y.L., Wang, Y., 2012. Talanta 98, 7–13.
Yan, F., Chen, H., Lü, Y., Lü, Z.H., Yu, S.C., Liu, M.H., Gao, C.J., 2016. J. Membr. Sci. 513, 108–116.
Yan, H.X., Tang, X.D., Zhu, X.D., Zeng, Y.B., Lu, X., Yin, Z.Z., Lu, Y.X., Yang, Y.W., Li, L., 2018. Sens. Actuators B 277, 234–240.
Yang, J.S., Pan, J., 2012. Acta Mater. 60, 4753–4758.
Yang, M.Q., Pan, X.Y., Zhang, N., Xu, Y.J., 2013. CrystEngComm 15, 6819–6828.
Yang, D.P., Guo, W.W., Cai, Z.F., Chen, Y.S., He, X.S., Huang, C.S., Zhuang, J.Y., Jia, N.Q., 2018. Sens. Actuators B 260, 642–649.
Yao, Y., Xue, M., Chen, J.Z., Zhang, M.M., Huang, F.H., 2012. J. Am. Chem. Soc. 134, 15712–15715.
Yao, Y., Xue, M., Zhang, Z.B., Zhang, M.M., Wang, Y., Huang, F.H., 2013. Chem. Sci. 4, 3667–3672.
Zhang, X.Y., Li, F., Wei, Q., Du, B., Wu, D., Li, H., 2014. Sens. Actuators B 194, 64–70.
Zhao, Y.B., Wang, Q., Li, J.X., Ma, H.M., Zhang, Y., Wu, D., Du, B., Wei, Q., 2016. J. Mater. Chem. B 4, 2963–2971.
Zhao, G.F., Ran, X., Zhou, X., Tan, X.P., Lei, H., Xie, X.G., Yang, L., Du, G.B., 2018. ACS Sustain. Chem. Eng. 6, 3938–3947.
Zheng, Y.B., Yang, Y.W., Jensen, L., Fang, L., Juluri, B.K., Flood, A.H., Weiss, P.S., Stoddart, J.F., Huang, T.J., 2009. Nano Lett. 9, 819–825.
Zhou, Q.Z., Zhang, B., Han, D.M., Chen, R.E., Qiu, F.L., Wu, J.S., Jiang, H.J., 2015. Chem. Commun. 51, 3124–3126.
Zhou, X., Yang, L., Tan, X.P., Zhao, G.F., Xie, X.G., Du, G.B., 2018. Biosens. Bioelectron. 112, 31–39.